

Accelerating Triple Transport in Zinc-Air Batteries and Water Electrolysis by Spatially Confining Co Nanoparticles in Breathable Honeycomb-Like Macroporous N-Doped Carbon

Haiyan Wang, Yakun Jiao, Saijun Wang, Pengcheng Ye, Jiqiang Ning, Yijun Zhong, and Yong Hu*

Rational engineering electrode structure to achieve an efficient triple-phase contact line is vital for applications such as in zinc-air batteries and water electrolysis. Herein, a facile “MOF-in situ-leaching and confined-growth-MOF” strategy is developed to construct a breathable trifunctional electrocatalyst based on N-doped graphitic carbon with Co nanoparticles spatially confined in an inherited honeycomb-like macroporous structure (denoted as Co@HMNC). The unique orderly arranged macroporous channels and the “ships in a bottle” confinement effect jointly expedite the triple transport, endowing the catalysts with fast reaction kinetics. As a result, the obtained Co@HMNC catalyst presents superb trifunctional performance with a positive half-wave potential ($E_{1/2}$) of 0.90 V for oxygen reduction reaction (ORR), and low overpotentials of 318 and 51 mV for oxygen evolution reaction (OER) and hydrogen evolution reaction (HER) at 10 mA cm⁻², respectively. The Co@HMNC-based liquid Zn-air battery reaches a large specific capacity of 859 mA h g_{Zn}⁻¹, a high-power density of 198 mW cm⁻², and long-term stability for 375 h, suggesting its promise for actual applications.

1. Introduction

Developing ecofriendly, efficient, and sustainable energy technologies is essential to address the grand challenge associated with the rapid increase in global energy demand and climate change.^[1] As representative innovative energy conversion

technologies, rechargeable Zn-air batteries featuring oxygen reduction reaction (ORR) and oxygen evolution reaction (OER),^[2] and water electrolyzers involving hydrogen evolution reaction (HER) and OER,^[3] are attracting renewed interest. However, their commercialization is primarily restricted by the inferior energy utilization efficiency, cyclic ability, and output power, which are stemmed from the sluggish kinetics and poor cycling stability of electrocatalysts. To date, Pt-based materials are still recognized as the best catalysts for HER and ORR, and the OER electrocatalysts are often derived from Ir- and Ru-based materials.^[4] Regardless of their “rare earth” status with high-cost, the inferior multifunctional performance and stability severely restrict their large-scale applications in clean energy devices.

Transition metal-based materials hybridized with N-doped carbon have become promising candidates for high-performance Zn-air batteries and water electrolysis in recent years.^[5] However, directly depositing active materials on an N-doped carbon matrix often leads to the loss or aggregation of metal nanoparticles (NPs).^[6] Spatially confining metal NPs in a sealed carbon shell provides a reasonable strategy to address this issue.^[7] Besides efficient control of NP size and protection of transition metal from erosion, the physicochemical properties of the catalysts and the electrocatalytic process in such a confined space can be changed by adjusting the coordination environments, tailoring the electronic structures, and modulating the adsorption of reaction intermediates.^[8] However, since HER, OER and ORR are triple-phase reactions involving gas, liquid, and solid phases, the absence of high porosity and the narrow mass diffusion channels in a carbon matrix usually make the pores easily blocked by electrolytes and the active metal species are difficult to “breathe”, especially those buried deep inside into the carbon matrix, leading to poor contact between oxygen/hydrogen gas, solid catalyst and liquid electrolyte and a low utilization of active sites.^[9] Recently, the “ship in a bottle” design that is confining metal NPs inside the channels or pores of porous materials, has been applied in electrochemical systems, which is demonstrated as an efficient way to alleviate this issue.^[10] Nevertheless, the carbon pore channels are often disordered, and therefore

H. Wang, Y. Jiao, S. Wang, P. Ye, Y. Zhong, Y. Hu
Key Laboratory of the Ministry of Education for Advanced Catalysis Materials
Department of Chemistry
Zhejiang Normal University
Jinhua 321004, China
E-mail: yonghu@zjnu.edu.cn, yonghuzjnu@163.com

J. Ning
Department of Optical Science and Engineering
Fudan University
Shanghai 200438, China

Y. Hu
Hangzhou Institute of Advanced Studies
Zhejiang Normal University
Hangzhou 311231, China

 The ORCID identification number(s) for the author(s) of this article can be found under <https://doi.org/10.1002/smll.202103517>.

DOI: 10.1002/smll.202103517

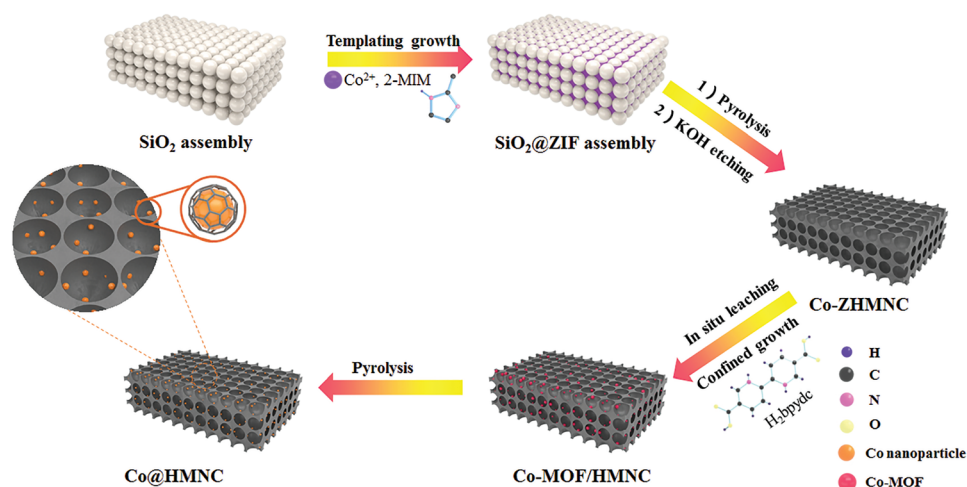


Figure 1. Schematic illustration of the “MOF-in situ-leaching and confined-growth-MOF” strategy for the synthesis of the Co@HMNC.

the mass transfer between the NPs inside the different pores is still not satisfactory. More efforts to pull through the barrier and achieve a better triple-phase contact line with well-balanced electron conduction, ion transportation, and gas diffusion are highly needed to improve the electrocatalytic performance.

Previous studies have reported that the pore structures and pore sizes of electrocatalysts are closely related to mass transfer and significantly influence the electrocatalytic process of OER, ORR, and HER.^[11] Building a 3D ordered structure with enough spacious and interconnected macropores could maximize the exposure of active sites, propel a continuous electronic transmission, and provide a direct pathway for gas permeation and electrolyte diffusion, all of which are favorable to the reaction kinetics.^[12] Generally, 3D ordered structure was fabricated by the formation of MOFs or ZIFs on the ordered template, followed by a high-temperature annealing procedure.^[13] To achieve well-dispersed metal/nitrogen-doped ordered macro-/mesoporous catalysts with excellent performance, the mass loading of metal was relatively low.^[13b] While a high loading of active components is essential for achieving a large current density for water electrolysis and a high power density in Zn-air batteries. Besides, by using this strategy, some active species may be buried by the carbon matrix, which is not conducive to the contact with gas and liquid electrolyte. It is still an enormous challenge to the construction of a highly active and durable multifunctional transition metal/N-doped carbon electrocatalyst integrating “ship in a bottle” confinement effect and a 3D well-arranged interconnected macroporous structure with trifunctional activities towards ORR, OER, and HER, but it is of great significance.

We herein demonstrate an efficient “MOF-in situ-leaching and confined-growth-MOF” strategy for the synthesis of a breathable trifunctional electrocatalyst based on N-doped graphitic carbon with Co NPs spatially confined in an inherited honeycomb-like macroporous structure (denoted as Co@HMNC) for accelerating triple transport in ORR, OER, and HER. Experiment results show that the two-step MOF growth strategy enables that numerous Co NPs safeguarded by N-doped carbon are immobilized onto the inner walls of macropores, which possess excellent uniformity even at a high Co content

of 29.56 wt.% and benefit to the exposure of active sites to electrolytes and protect the metals from dissolution and agglomeration in a confined environment. Moreover, the honeycomb-like macroporous channels provide continuous direct pathways, expediting gas diffusion, and speeding electron and electrolyte transport throughout the catalyst. Each interconnected macropore works like an “alveolus” reactor for electrocatalytic reactions, and ensures the interior NPs smoothly “inhale” reactants or “exhale” products. As a result, the as-prepared breathable Co@HMNC catalyst exhibits a superior trifunctional electrocatalytic ability with a more positive half-wave potential ($E_{1/2}$) of 0.90 V for ORR, and lower overpotentials of 318 and 51 mV for OER and HER at 10 mA cm⁻², respectively, compared to those of Co-based honeycomb-like macroporous N-doped carbon obtained through one-step ZIF-67 growth method under pyrolysis at 700 °C (denoted as Co-ZHMNC-700) and ZIF-67 polyhedron crystal derived Co NPs encapsulated in N-doped carbon (Co@NC nanohybrids). The as-assembled liquid Zn-air battery using Co@HMNC as the air electrode achieves a large specific capacity of 859 mA h g_{Zn}⁻¹, a high-power density of 198 mW cm⁻² and long-term stability for 375 h. Additionally, the solid-state Zn-air battery based on the catalyst delivers a high-power density of 107 mW cm⁻², illustrating its great potential for energy-related technologies.

2. Results and Discussion

The synthetic procedure for Co@HMNC by using a simple “MOF-in situ-leaching and confined-growth-MOF” strategy is schematically illustrated in **Figure 1**. Monodispersed SiO₂ nanospheres with an average diameter of about 200 nm were first self-assembled through a centrifuge process (Figures S1 and S2, Supporting Information). After soaking SiO₂ template in Co(NO₃)₂ solution, the SiO₂ nanospheres were modified with Co²⁺ ions, which further provided abundant nucleation sites for ZIF-67. The subsequent immersion of SiO₂/Co(NO₃)₂ into 2-methylimidazole (2-MIM) methanol solution induced the uniform deposition of a thin layer of ZIF-67 in the voids of SiO₂ assembly (SiO₂@ZIF-67, Figure S1c,S1d, Supporting Information).

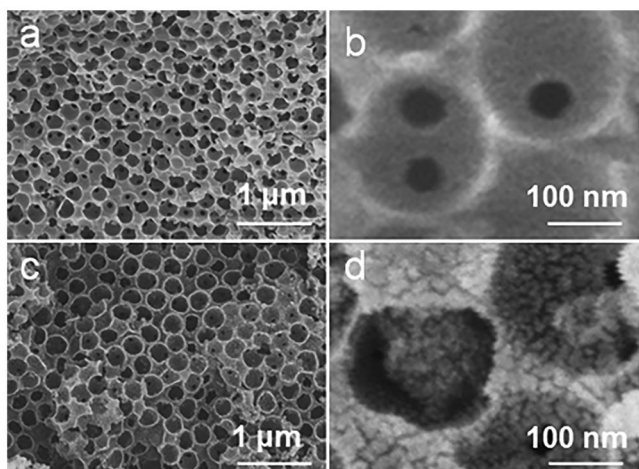


Figure 2. a) SEM and b) the enlarged SEM images of the Co-ZHMNC. c) SEM and d) the enlarged SEM images of the Co@HMNC.

Figure S3a, Supporting Information, shows the typical X-ray diffraction (XRD) pattern of SiO₂@ZIF-67, proving the successful synthesis of ZIF-67. During the pyrolysis in N₂ atmosphere at 500 °C, ZIF-67 decomposed slowly, which was further converted to a N-doped carbonous framework padding in the interspace of the SiO₂ template with uniformly dispersed cobalt ions in the carbon matrix. After removal of SiO₂ with KOH, Co-ZHMNC product with a honeycomb-like N-doped macroporous structure was obtained. As **Figure 2a** show, Co-ZHMNC sample exhibits interconnected macropores with a diameter of ≈200 nm, corresponding to the size of SiO₂. It can be obviously seen that these macropores in Co-ZHMNC exhibit a smooth surface (**Figure 2b**). The XRD pattern depicts the typical peaks of graphitic carbon but without the characteristic peaks for Co-based species, suggesting the nonexistence of Co metal (**Figure S3b**, Supporting Information). The pore confinement of Co@HMNC catalyst was further realized by in situ leaching of Co-ZHMNC under acid condition and confined growth of Co-MOF in the well-arranged honeycomb-like macropores, followed by a pyrolysis procedure. 2,2'-bipyridyl-5,5'-dicarboxylic acid (H₂bpydc) ligand first reacted with the in situ dissolved Co²⁺ ions to form Co-MOF,^[14] which then nucleated and grew up in the honeycomb-like N-doped macroporous carbon (Co-MOF/HMNC). H₂bpydc with abundant functional groups such as 2,2-bipyridine and carboxyl groups to coordinate with metal ions possesses outstanding advantages as the ligand for the secondary MOF synthesis.^[15] Besides, the Co-MOF synthesized with H₂bpydc ligand usually exhibits excellent stability in acid solution, which enables the successful formation of Co-MOF/HMNC.^[14,16] As the content of ligand increases, the inner wall of the macropore becomes rougher and thicker because much more Co-MOFs are formed (**Figures S4 and S5**, Supporting Information). Finally, after annealing in N₂ atmosphere at 700 °C, the Co-MOF was converted into N-doped graphitic carbon layers encapsulated with Co NPs, which were confined in a honeycomb-like macroporous N-doped carbon matrix (denoted as Co@HMNC-X, X represents the content of ligand) (**Figure 2c** and **Figure S6**, Supporting Information). As shown in **Figure 2d**, numerous NPs grow firmly onto the inner walls of the well-arranged interconnected macropores, which

is clearly different from SiO₂@ZIF-67 derived Co-ZHMNC-700 (**Figures S7 and S8**, Supporting Information). In addition, to have an in-depth understanding of the important role of the confinement effect, ZIF-67 polyhedron crystal derived Co@NC nanohybrids were also synthesized for comparison, evidencing that the honeycomb-like 3D interconnected macroporous N-doped carbon matrix structure could prominently inhibit the aggregation of Co NPs at high temperature, highly improve the mechanical stability, and accelerate mass transfer as well as avail the primary exposure of abundant active sites (**Figures S9 and S10**, Supporting Information).

The 3D honeycomb-like configuration of Co@HMNC sample was further investigated by transmission electron microscopy (TEM), which explicitly reveals well-arranged interconnected macropores with diameters of nearly 200 nm, corresponding to the size of silica template (**Figure 3a**). The magnified TEM image shows that a large number of NPs with an average size of ≈10–11 nm in diameter are homogeneously embedded in the carbonous macropores, verifying the crucial role of pore confinement in preventing Co NPs from agglomeration (**Figure 3b** and **Figure S11**, Supporting Information). Obviously, these NPs have a core-shell structure with a well-crystallized metallic Co core and an ultrathin graphitic carbon shell layer (**Figure 3c**). In addition, the corresponding selected-area electron diffraction (SAED) pattern displays the different diffraction planes of Co metal, suggesting that Co-MOF are entirely fully converted into metallic Co after pyrolysis (**Figure 3d**). Elemental mapping also unveils that Co, C, and N elements spatially homogeneously distribute throughout the honeycomb-like interconnected Co@HMNC catalyst (**Figure 3e–3h**). The high-resolution energy dispersive spectroscopy images of the Co@HMNC indicates that the C element distributes throughout the macroporous carbon matrix, while Co element is dispersed in the hole, corresponding to the conclusion of the high-resolution SEM images that the Co NPs are distributed on the inner walls of the matrix (**Figure S12**, Supporting Information).

The phase structures of the as-prepared Co@HMNC-X catalysts were further investigated by XRD and Raman measurements. Except for the peak at 26.5° for graphitic carbon, all the samples display the typical characteristic diffraction peaks of Co (JCPDS No. 15–0806), which are consistent with the high-resolution transmission electron microscopy (HRTEM) results (**Figure 4a**). Raman spectra show two peaks located at ≈1350 and 1590 cm⁻¹, which can be ascribed to the D-band of defective carbon and the G-band of graphitic carbon, respectively (**Figure 4b**).^[17] The similar I_D/I_G ratio implies a similar graphitization and defect degree of the samples. The chemical compositions and bonding configurations of the as-prepared Co@HMNC sample were further investigated by X-ray photoelectron spectroscopy (XPS). The survey spectrum of the Co@HMNC manifests the existence of C, N, O, and Co elements with the surface percentages of 75.2%, 11.1%, 11.4%, and 2.3%, respectively (**Figure S13**, Supporting Information). Compared to that of Co-ZHMNC-700 (6.9% of N), the higher content of N is introduced by the secondary MOF growth strategy with H₂bpydc as the ligand, which may activate the metal core and enhance the oxygen electrocatalytic performance (**Table S1**, Supporting Information).^[8d,18] As shown in **Figure 4c**, the high-resolution Co 2p XPS spectrum can be fitted with three

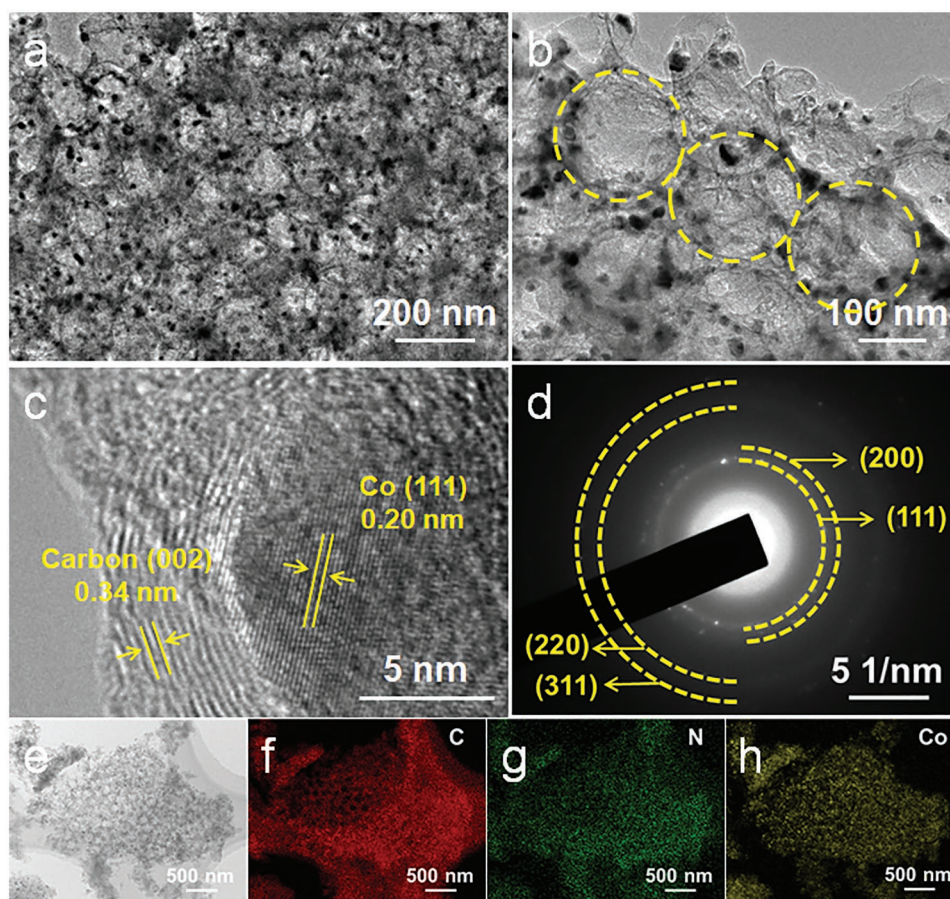


Figure 3. a,b) TEM images, c) HRTEM image, and d) the corresponding SAED pattern of the Co@HMNC. e) STEM image of the Co@HMNC, and the corresponding elemental mapping images of f) C, g) N, and h) Co elements.

types of Co species that are metallic Co (778.5 and 793.2 eV), Co^{3+} (780.1 and 795.7 eV), and Co^{2+} (781.9 and 797.7 eV) with two satellite peaks at 785.7 and 803.1 eV corresponding to Co^{2+} .^[19] The deconvoluted N 1s XPS spectrum (Figure 4d) shows five main peaks at 398.5, 399.2, 400.2, 401.1, and 402.4 eV, which are attributed to the pyridinic N, Co–N_x, pyrrolic N, graphitic N, and oxidized N species, respectively.^[19] The existence of Co–N_x species suggests the strong interactions between Co NPs and N-doped graphitic carbon layers, which are believed to reduce the energy barrier and improve the electrocatalytic activity for OER/ORR.^[20] Evidently, Co@HMNC exhibit higher contents of Co–N and pyridinic/graphitic N species, which are believed to avail the breaking and formation of O=O bonds, so as to promote the ORR and OER processes (Figure S14 and Table S2, Supporting Information).^[21]

N₂ adsorption-desorption test was then conducted to reveal the pore structure of the as-prepared Co@HMNC catalyst, which exhibits the typical type IV isotherm with an H3 hysteresis loop, as shown in Figure 4e. A large adsorption capacity in the medium-pressure and high-pressure regions is found, manifesting the existence of abundant mesopores and macropores in Co@HMNC. In contrast, Co@NC nanohybrids show similar isotherms except for the prominent characteristics of mesopores and macropores. A Brunauer–Emmett–Teller (BET) specific surface area of 369 m² g^{−1} is achieved for

the Co@HMNC, which is higher than 113 and 19 m² g^{−1} of Co-ZHMNC-700 and Co@NC nanohybrids, respectively. The larger specific surface area may be attributed to the subsequent “MOF-in situ-leaching and confined-growth-MOF” process, which induces much micropores and mesopores in the Co@HMNC (Figure 4f). Large micropore volume of 0.15 cm³ g^{−1} and meso-/macropore volume of 0.3 cm³ g^{−1} are also achieved for Co@HMNC, which are significantly higher than those of Co-ZHMNC-700 and Co@NC nanohybrids (Table S3, Supporting Information). The pore size distribution also certifies the hierarchical pore structure of Co@HMNC with micropores centered at 1.7 nm and mesopores centered at 4.3 nm. The macropores are generated by removing the SiO₂ template, and the micropores, and small mesopores may result from the gas (e.g. H₂O, CO₂) release via decomposition of ligand, resulting in a hierarchical porous structure in the Co@HMNC.^[22] It is worth noting that the large specific surface area and the hierarchical pores could benefit to the exposure of rich active sites, favor the permeation of electrolyte ions as well as facilitate the access and release of gas, thus expecting to achieve fast reaction kinetics at the three-phase interface and display an enhanced electrocatalytic performance.^[20,23]

To evaluate the electrocatalytic activities of the as-prepared catalysts, their ORR performances were first investigated using a three-electrode configuration in 0.1 M KOH solution. For com-

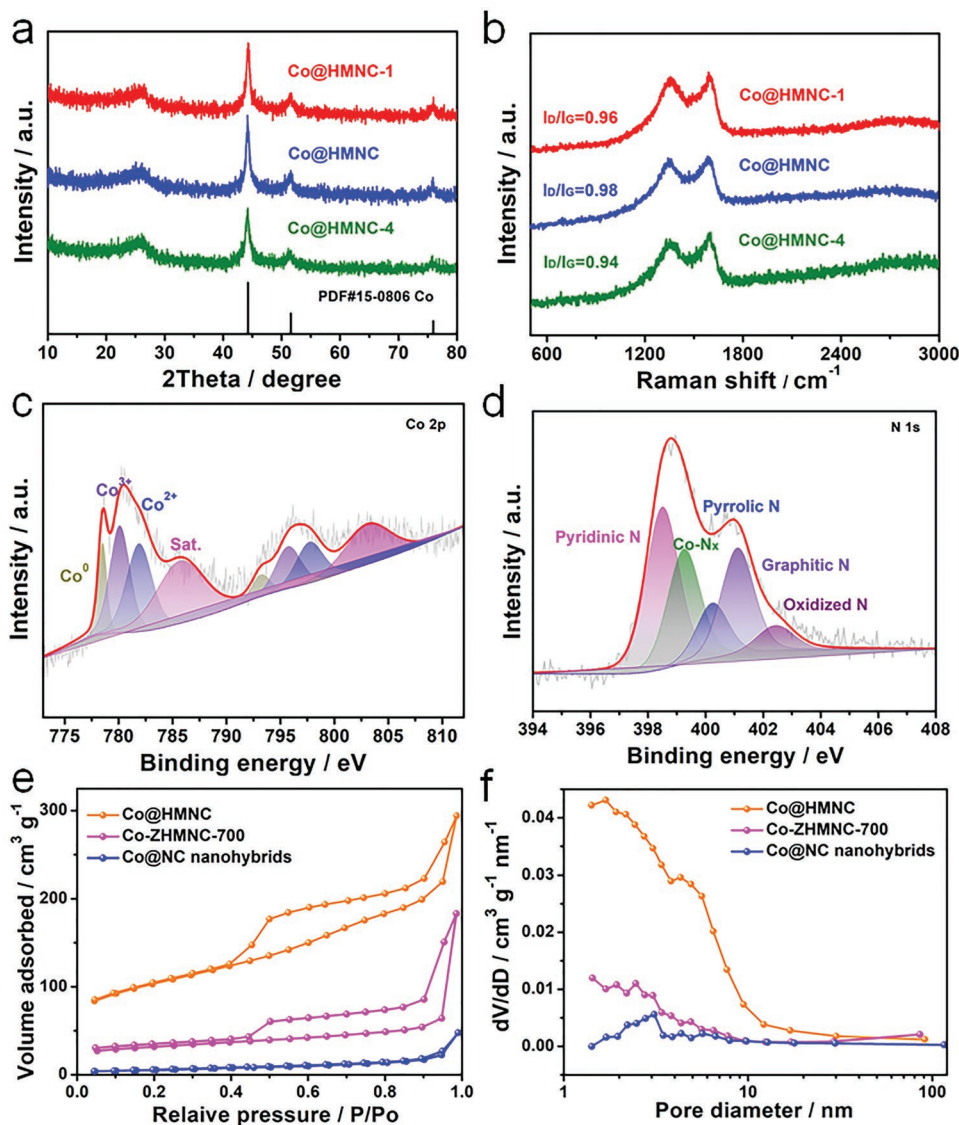


Figure 4. a) XRD patterns of the as-prepared Co@HMNC-1, Co@HMNC, and Co@HMNC-4 samples. b) Raman spectra of the Co@HMNC-1, Co@HMNC, and Co@HMNC-4. High-resolution c) Co 2p and d) N 1s XPS spectra of the Co@HMNC. e) N_2 adsorption and desorption curves and f) pore size distributions of the Co@HMNC, Co-ZHMNC-700, and Co@NC nano hybrids.

parison, Co-ZHMNC-700, Co@NC nano hybrids, and commercial Pt/C catalysts were also evaluated under the same condition. The cyclic voltammetry (CV) curve (Figure S15, Supporting Information) of Co@HMNC in O_2 -saturated 0.1 M KOH electrolyte presents an obvious oxygen reduction peak, while the cathodic peak is absent under N_2 -saturated condition, implying an emblematic ORR activity. As observed in the linear sweep voltammetry (LSV) curves, Co@HMNC exhibits the most positive $E_{1/2}$ of 0.90 V and surpasses the contrast samples including Co-ZHMNC-700 (0.83 V), Co@NC nano hybrids (0.655 V), and Pt/C (0.85 V) catalysts and most reported trifunctional catalysts (Figure 5a, Figure S16a, and Table S4, Supporting Information), demonstrating the as-prepared Co@HMNC with abundant Co NPs confined in the 3D well-arranged honeycomb-like interconnected macroporous architecture for providing more active sites and enhancing the ORR process. The lower limiting

current density of Co-ZHMNC-700 may be ascribed to the lower content of graphitic N and the smaller electrochemical active surface area (ECSA) compared to those of Co-ZHMNC-700.^[24] The advantage of Co@HMNC for promoting the ORR kinetics could also be seen from the relatively lower Tafel slope of 64 $mV\ dec^{-1}$ in comparison with the other samples (Figure 5b and Figure S16b, Supporting Information). Rotating ring-disk electrode (RRDE) results reveal that the H_2O_2 yields for Co@HMNC are below 1.3% at the potential ranging from 0.2 to 0.8 V and the calculated electron transfer numbers (n) are between 3.90 and 4.00 (Figure S17, Supporting Information). These results are in accordance with the Koutecky–Levich (K–L) plot obtained from the LSV curves at different rotation rates from 400 to 2500 rpm, further verifying the effective four-electron ORR pathway in alkaline medium (Figure S18, Supporting Information). Moreover, the Co@HMNC catalyst displays a

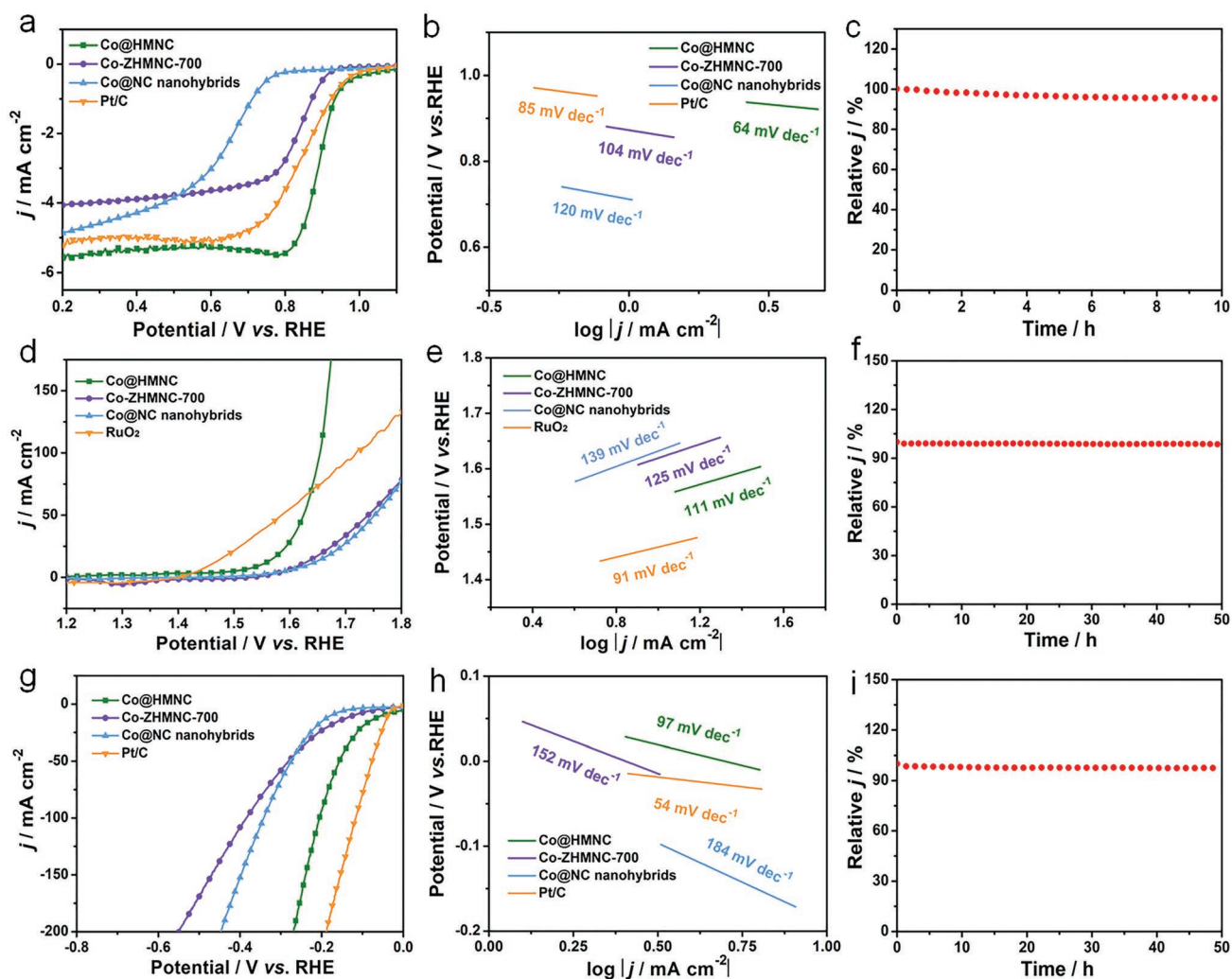


Figure 5. Evaluation of the ORR, OER, and HER performances of the as-prepared Co@HMNC, Co-ZHMNC-700, Co@NC nano hybrids, and commercial Pt/C or RuO₂ catalysts. a) ORR LSV curves in 0.1 M KOH. b) ORR Tafel plots. c) ORR stability test of Co@HMNC. d) OER LSV curves in 1 M KOH. e) OER Tafel plots. f) OER stability test of Co@HMNC. g) HER LSV curves in 1 M KOH. h) HER Tafel plots. i) HER stability test of Co@HMNC.

current retention of more than 95% after 10 h continuous chronoamperometric test (Figure 5c), suggesting its robust durability for ORR. These results clearly demonstrate that the Co@HMNC catalyst possesses eminent activity and remarkable stability toward ORR in alkaline media.

The electrochemical OER and HER properties of Co@HMNC-X catalysts were further examined in 1 M KOH electrolyte with Co-ZHMNC-700, Co@NC nano hybrids, and RuO₂ as comparisons. The catalysts were first coated on Ni foam for evaluating their OER and HER performances. The OER LSV curve of Co-ZHMNC-700 exhibits a weak broad peak between 1.2–1.4 V, which is due to the reduction of the high-valence cobalt ions on the surface during the reverse sweep. Co@HMNC displays an overpotential of 318 mV to achieve a current density of 10 mA cm⁻², which is superior to Co@HMNC-1 (380 mV), Co@HMNC-4 (372 mV), Co-ZHMNC-700 (389 mV), and Co@NC nano hybrids (402 mV) and comparable to the reported trifunctional catalysts (Figure 5d, Figure S19a and Table S4, Supporting Information). Additionally, a much smaller Tafel slope of

111 mV dec⁻¹ is achieved with the Co@HMNC catalyst in comparison with those of Co@HMNC-1, Co@HMNC-4, Co-ZHMNC-700, and Co@NC nano hybrids, indicating an accelerated OER kinetics and interface reactions (Figure 5e and Figure S19b, Supporting Information). These results are in accordance with that obtained from electrochemical impedance spectroscopy, where Co@HMNC exhibits the smallest charge transfer resistance (*R*_{ct}) among the samples, suggesting the fastest charge transfer kinetics (Figure S20, Supporting Information). As Figure 5f depicted, Co@HMNC catalyst exhibits a preminent OER stability for 50 h with a negligible degradation of current density. Similar to ORR and OER activities, the Co@HMNC catalyst presents a preferable HER activity to those of Co-ZHMNC-700, Co@NC nano hybrids, and other Co@HMNC-X catalysts, achieving 10 mA cm⁻² at a low overpotential of 51 mV (Figure 5g and Figure S21a, Supporting Information). The value is also superior or comparable to the best results for the reported trifunctional catalysts (Table S4, Supporting Information). The Tafel slope for Co@HMNC is calculated to be 97 mV dec⁻¹,

smaller than 147 mV dec^{-1} for Co@HMNC-1, 135 mV dec^{-1} for Co@HMNC-4, 152 mV dec^{-1} for Co-ZHMNC-700, and 184 mV dec^{-1} for Co@NC nanohybrids (Figure 5h and Figure S21b, Supporting Information). Moreover, the Nyquist plots show a noticeably smaller R_{ct} for Co@HMNC compared to those of the other samples, suggesting an accelerated HER kinetics for HER (Figure S22, Supporting Information)^[25]. The electrocatalytic stability for hydrogen evolution is depicted in Figure 5i, where Co@HMNC holds the current density of 10 mA cm^{-2} over 50 h, indicating a superb stability for HER. Moreover, the OER and HER performances of the Co@HMNC were also tested on a rotating disk electrode (RDE) to further verify the trifunctional performance of the catalyst. Figure S23, Supporting Information, shows the OER and HER polarization curves of Co@HMNC tested on RDE (Co@HMNC/RDE). The Co@HMNC/RDE displays the overpotentials of 336 and 80 mV at a current density of 10 mA cm^{-2} for OER and HER, respectively, verifying the excellent trifunctional performance of the Co@HMNC catalyst. The slight difference between Co@HMNC coated on Ni foam and the Co@HMNC/RDE may be ascribed to the following reasons. First, 3D porous substrates can offer a larger electrode and electrolyte contact area than that of a planar substrate like glass carbon electrode.^[26] Second, the porous structure could facilitate ionic transport and improve the ESCA.^[27] Third, the higher loading of catalysts on metal foam can reduce the overpotential at 10 mA cm^{-2} .^[28]

Furthermore, the ECSA is an essential parameter for affecting the catalytic activity of electrocatalysts. To better comprehend the underlying reasons for the superior electrocatalytic performance of Co@HMNC, the double layer capacitance (C_{dl}) was used to evaluate the ECSA of the samples due to their linear relation (Equation S5, Supporting Information). The C_{dl} can be calculated by the CV curves at different scan rates in a narrow potential range without Faradaic reaction. Therefore, a larger C_{dl} manifests a larger ECSA and more active sites. As displayed in Figures S24 and S25, Supporting Information, Co@HMNC shows the largest double layer capacitance (C_{dl}) of 73 mF cm^{-2} among the samples, much higher than 19 mF cm^{-2} for Co-ZHMNC-700 and 15 mF cm^{-2} for Co@NC nanohybrids, indicating that the Co@HMNC catalyst has a larger ECSA and can expose more catalytically active sites to the electrolytes. In addition, acid etching experiment was also carried out to investigate the effect of Co NPs on the electrochemical properties of the Co@HMNC catalyst. The corresponding energy-dispersive X-ray spectroscopy (EDX) results show that a great mass of metallic Co NPs is removed after acid etching (Figure S26, Supporting Information). As a result, the Co@HMNC catalyst after acid etching exhibits inferior ORR, OER, and HER activities compared to the original sample, indeed verifying that metallic Co participated actively in the ORR, OER, and HER (Figure S27, Supporting Information). Hence, the outstanding trifunctional performance of the as-prepared Co@HMNC catalyst could be attributed to the following reasons. For one, the well-arranged 3D interconnected macroporous architecture with hierarchical pores and large specific surface area prominently increases the ECSA, favors the access and release of gas (O_2 or H_2), accelerates the electrolyte transport at the three-phase interface, as well as avails the exposure of abundant active sites, all of which are extremely beneficial for electrocata-

lytic ORR, OER, and HER. For another, the metallic Co NPs safeguarded by N-doped carbon are immobilized on the inner wall of macropores firmly. This unique structure not only conduces to the contact between active sites and the reactants, and improves the electron/charge transfer process by introducing conductive carbon and Co metal, but also critically inhibits the aggregation and detachment of Co NPs, thus boosting the activity, stability, and durability for electrocatalytic reactions. Last but not the least, the rich metallic Co active sites and relatively high nitrogen content, as well as abundant Co–N species in Co@HMNC synergistically accelerate the reaction kinetics of ORR, OER, and HER. Previous studies have found that the C active sites in the Co–N–C structure possess ORR activity, while the Co sites show OER activity, which enables the outstanding ORR/OER activities.^[29] Besides, the Co and N sites in Co/NC, cooperated with C active sites are favorable for the formation/decomposition of OOH^* and O^* intermediates, thus efficiently boosting the ORR/OER kinetics.^[29a] In addition, the Co*/N-C* biactive sites in such a Co/N-C hybrid catalyst system can efficiently promote the dissociation of $\text{H}_{ads}\text{-OH}$ and accelerate the formation of C– H_{ads} , thus enhancing the HER kinetics.^[30]

The potential difference between the OER potential at 10 mA cm^{-2} ($E_{j=10}$) and the $E_{1/2}$ of ORR ($\Delta E = E_{j=10} - E_{1/2}$) could provide a view of the bifunctional performance of the catalysts. Notably, the Co@HMNC catalyst exhibits a lower ΔE of 0.648 V in comparison with Co-ZHMNC-700 (0.789 V) and Co@NC nanohybrids (0.977 V), indicating a superior bifunctional property. Considering the excellent bifunctional electrocatalytic activity for ORR and OER, the as-prepared Co@HMNC catalyst was subsequently applied as the air cathode to construct a rechargeable Zn-air battery. As shown in Figure S28, Supporting Information, the assembled liquid Zn-air battery with Co@HMNC catalyst delivers a large open-circuit voltage of 1.49 V. A large specific capacity of $859 \text{ mA h g}_{\text{Zn}}^{-1}$ at 20 mA cm^{-2} is also achieved with Co@HMNC, which is superior to that based on Co-ZHMNC-700 ($781 \text{ mA h g}_{\text{Zn}}^{-1}$) and Co@NC nanohybrids ($691 \text{ mA h g}_{\text{Zn}}^{-1}$), and among the best values for the reported Zn-air batteries (Figure 6a and Table S5, Supporting Information). In addition, galvanostatic discharge results reveal that the Co@HMNC-based liquid Zn-air battery also exhibits a good rate capability with a rapid dynamic response when the current density ranges from 2 to 20 mA cm^{-2} (Figure S29, Supporting Information). Moreover, the Co@HMNC-based Zn-air battery affords a much higher power density of 198 mW cm^{-2} at 326 mA cm^{-2} compared to that based on Pt/C and RuO_2 (Figure 6b). Stability is another critical criterion to evaluate the application prospects of a rechargeable Zn-air battery. The stable voltage plateau in the galvanostatic discharging-charging curve can be maintained well for 375 h at 10 mA cm^{-2} , far surpassing that of Co-ZHMNC-700 and Co@NC nanohybrids-based devices, and also comparable to the long-term durability of the rechargeable Zn-air batteries (Figure 6c, Figures S30 and S31 and Table S6, Supporting Information). SEM image shows that the 3D honeycomb-like macroporous structure of the Co@HMNC catalyst is maintained after long-term stability test (Figure S32, Supporting Information). In addition, the XRD pattern of the Co@HMNC after long cycle test exhibits the characteristic peaks of graphitic carbon and metallic Co, which is consistent with

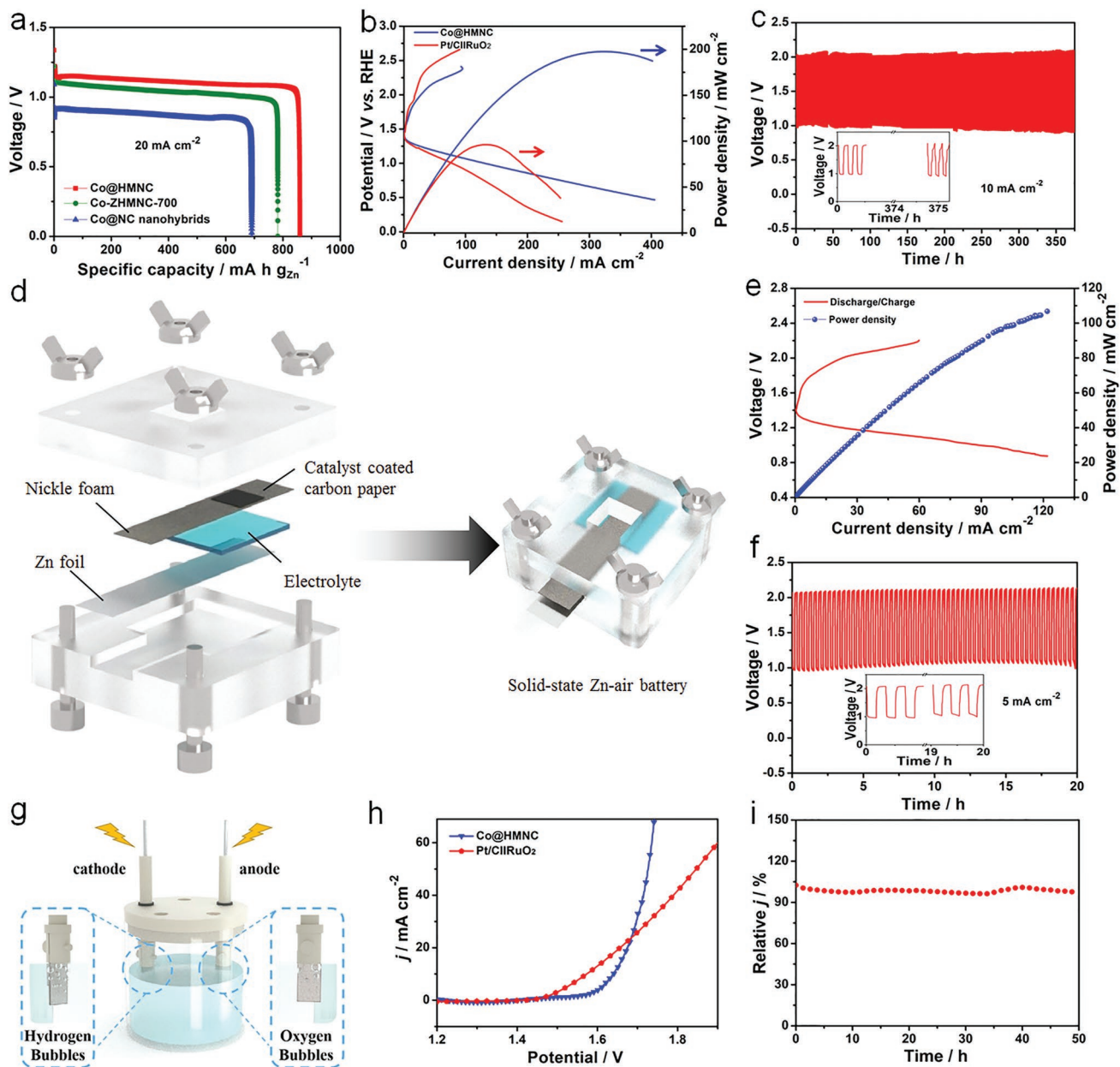


Figure 6. Evaluation of the as-assembled liquid Zn-air battery, solid-state Zn-air battery, and water electrolyzer. a) Specific capacities of the Co@HMNC, Co-ZHMNC-700, and Co@NC nano hybrids-based liquid Zn-air batteries. b) Charge and discharge curves and power densities of the liquid Zn-air batteries using Co@HMNC, and Pt/C||RuO₂ catalysts. c) Cycling stability of Co@HMNC-based liquid Zn-air battery at 10 mA cm⁻² with an inset of the charge-discharge curves at the beginning and end of cycle life. d) Schematic illustration of the as-assembled solid-state Zn-air battery. e) Charge and discharge curves and power densities of the Co@HMNC-based solid-state Zn-air battery. f) Cycling stability of the Co@HMNC-based solid-state Zn-air battery at 5 mA cm⁻² with an inset of the charge-discharge curves at the beginning and end of cycle life. g) Schematic illustration of the water electrolyzer. h) LSV curves of the water electrolyzers using Co@HMNC and Pt/C||RuO₂. i) Cycling stability of Co@HMNC-based water electrolyzer.

the original catalyst, further verifying the excellent stability of the as-prepared Co@HMNC catalyst (Figure S33, Supporting Information). Driven by the increasing demand for portable electronics, a homemade solid-state Zn-air battery was fabricated with Co@HMNC supported on a carbon paper as the air cathode, Zn foil as the anode, and polyvinyl alcohol/KOH/Zn(OAc)₂ hydrogel as the solid-state electrolyte (Figure 6d). As expected, the solid-state Zn-air battery exhibits an open-circuit

voltage of 1.41 V and a high power density of 107 mW cm⁻² (Figure S34, Supporting Information and Figure 6e). Two solid-state Zn-air batteries connected in series are capable of powering a red light-emitting diode (LED) and a small fan (inset of Figure S34, Supporting Information). Besides, the long-term cycling performance at 5 mA cm⁻² further proves its robust stability, where a negligible change in charging-discharging voltage gap can be observed over 20 h test (Figure 6f). In light

of the prominent electrocatalytic activities and stabilities for OER and HER, Co@HMNC catalysts were then utilized as both the anode and cathode to fabricate an alkaline water electrolysis system (Figure 6g). The assembled alkaline water electrolyzer delivers the current density of 10 mA cm^{-2} at a voltage of 1.64 V, and exhibits good long-time stability with a small fluctuation of the current density during 50 h continuous water electrolysis (Figure 6h,6i). Thus, we can conclude that the as-prepared Co@HMNC catalyst with the unique structure and rich active sites is a promising alternative for Zn-air batteries and alkaline water electrolyzers.

3. Conclusion

In summary, we have presented an effective “MOF-in situ-leaching and confined-growth-MOF” strategy to fabricate a breathable trifunctional electrocatalyst based on N-doped graphitic carbon with Co NPs spatially confined in an inherited honeycomb-like macroporous structure. The well-arranged honeycomb-like macroporous channels and the “ships in a bottle” confinement effect jointly expedite the triple transport, endowing the catalysts with fast electrocatalytic reaction kinetics. Besides, the large specific surface area, the rich metallic Co active sites, and relatively high nitrogen content, as well as abundant Co–N species in the Co@HMNC catalyst could provide more active sites for electrocatalysis. As expected, the breathable Co@HMNC catalyst presents a superior trifunctional performance with a positive $E_{1/2}$ of 0.90 V for ORR, and low overpotentials of 318 and 51 mV for OER and HER at 10 mA cm^{-2} , respectively. The Co@HMNC-based liquid Zn-air battery reaches a large specific capacity of $859 \text{ mA h g}_{\text{Zn}}^{-1}$ at 20 mA cm^{-2} , a high-power density of 198 mW cm^{-2} and long-term stability for 375 h. Additionally, a solid-state Zn-air battery assembled with the catalyst delivers a high-power density of 107 mW cm^{-2} , suggesting its promise for actual applications. This strategy can open a new horizon for the fabrication of high-performance trifunctional electrocatalysts for sustainable energy devices.

Supporting Information

Supporting Information is available from the Wiley Online Library or from the author.

Acknowledgements

H.W., Y.J., and S.W. contributed equally to this work. Y.H. acknowledges the financial support from Natural Science Foundation of China (21671173), the Independent Designing Scientific Research Project of Zhejiang Normal University (2020ZS03), and Zhejiang Provincial Ten Thousand Talent Program (2017R52043).

Conflict of Interest

The authors declare no conflict of interest.

Data Availability Statement

Research data are not shared.

Keywords

Co nanoparticles, honeycomb-like macroporous carbon, triple transport, water electrolysis, Zn-air batteries

Received: June 16, 2021

Revised: September 16, 2021

Published online: November 1, 2021

- [1] a) X. Huang, Q. Meng, H. Chen, X. Du, L. Chen, *Science* **2018**, *360*, 47; b) H. Wang, W. Ye, Y. Yang, Y. Zhong, Y. Hu, *Nano Energy* **2021**, *85*, 105942; c) H. Wang, Y. Yang, Q. Li, W. Lu, J. Ning, Y. Zhong, Z. Zhang, Y. Hu, *Sci. China Mater.* **2021**, *64*, 840; d) B. Cui, X. Han, W. Hu, *Small Struct.* **2021**, *2*, 2000128.
- [2] a) H. J. Qiu, P. Du, K. Hu, J. Gao, H. Li, P. Liu, T. Ina, K. Ohara, Y. Ito, M. Chen, *Adv. Mater.* **2019**, *31*, 1900843; b) T. Zhou, N. Zhang, C. Wu, Y. Xie, *Energy Environ. Sci.* **2020**, *13*, 1132.
- [3] a) E. Hu, Y. Feng, J. Nai, D. Zhao, Y. Hu, X. W. Lou, *Energy Environ. Sci.* **2018**, *11*, 872; b) X. Luo, P. Ji, P. Wang, R. Cheng, D. Chen, C. Lin, J. Zhang, J. He, Z. Shi, N. Li, S. Xiao, S. Mu, *Adv. Energy Mater.* **2020**, *10*, 1903891.
- [4] a) L. Jiao, R. Zhang, G. Wan, W. Yang, X. Wan, H. Zhou, J. Shui, S. H. Yu, H. L. Jiang, *Nat. Commun.* **2020**, *11*, 2831; b) J. Diao, Y. Qiu, S. Liu, W. Wang, K. Chen, H. Li, W. Yuan, Y. Qu, X. Guo, *Adv. Mater.* **2020**, *32*, 1905679; c) J. Wang, T. Liao, Z. Wei, J. Sun, J. Guo, Z. Sun, *Small Methods* **2021**, *5*, 2000988.
- [5] a) M. Zhang, Q. Dai, H. Zheng, M. Chen, L. Dai, *Adv. Mater.* **2018**, *30*, 1705431; b) L. Yan, H. Wang, J. Shen, J. Ning, Y. Zhong, Y. Hu, *Chem. Eng. J.* **2021**, *403*, 126385; c) Y. Jiao, C. Yang, H. Wang, Y. Zhong, Y. Hu, *J. Alloys Compd.* **2021**, *890*, 161929; d) J. Zhang, M. Zhang, Y. Zeng, J. Chen, L. Qiu, H. Zhou, C. Sun, Y. Yu, C. Zhu, Z. Zhu, *Small* **2019**, *15*, 1900307.
- [6] a) Y. Tian, L. Xu, M. Li, D. Yuan, X. Liu, J. Qian, Y. Dou, J. Qiu, S. Zhang, *Nano-Micro Lett.* **2021**, *13*, 3; b) P. Tan, B. Chen, H. Xu, W. Cai, W. He, M. Chen, M. Ni, *J. Electrochem. Soc.* **2019**, *166*, 616.
- [7] a) L. Yan, Z. Xu, W. Hu, J. Ning, Y. Zhong, Y. Hu, *Nano Energy* **2021**, *82*, 105710; b) B. Y. Xia, Y. Yan, N. Li, H. B. Wu, X. W. Lou, X. Wang, *Nat. Energy* **2016**, *1*, 15006; c) S. Wang, H. Wang, J. Ning, Y. Zhong, Y. Hu, *Appl. Catal., B* **2021**, *298*, 120512.
- [8] a) T. Zheng, J. Jiang, J. Wang, S. Hu, W. Ding, Z. Wei, *Acta Phys. Chim. Sin.* **2021**, *37*, 2011027; b) C. Chen, Y. Li, D. Cheng, H. He, K. Zhou, *ACS Appl. Mater. Interfaces* **2020**, *12*, 40415; c) S. Chen, J. Duan, J. Ran, M. Jaroniec, S. Z. Qiao, *Energy Environ. Sci.* **2013**, *6*, 3693; d) W. Wang, Q. Jia, S. Mukerjee, S. Chen, *ACS Catal.* **2019**, *9*, 10126.
- [9] a) Y. He, S. Hwang, D. A. Cullen, M. A. Uddin, L. Langhorst, B. Li, S. Karakalos, A. J. Kropf, E. C. Wegener, J. Sokolowski, M. Chen, D. Myers, D. Su, K. L. More, G. Wang, S. Litster, G. Wu, *Energy Environ. Sci.* **2019**, *12*, 250; b) S. Dou, X. Wang, S. Wang, *Small Methods* **2019**, *3*, 1800211.
- [10] a) Z. Zhang, Y. P. Deng, Z. Xing, D. Luo, S. Sy, Z. P. Cano, G. Liu, Y. Jiang, Z. Chen, *ACS Nano* **2019**, *13*, 7062; b) Z. Zhang, G. Wen, D. Luo, B. Ren, Y. Zhu, R. Gao, H. Dou, G. Sun, M. Feng, Z. Bai, A. Yu, Z. Chen, *J. Am. Chem. Soc.* **2021**, *143*, 6855; c) Z. Xing, Y. P. Deng, S. Sy, G. Tan, A. Li, J. Li, Y. Niu, N. Li, D. Su, J. Lu, Z. Chen, *Nano Energy* **2019**, *65*, 104051; d) Q. Zhu, Q. Xu, *Chem* **2016**, *1*, 220.

- [11] a) T. Zhou, H. Shan, H. Yu, C. Zhong, J. Ge, N. Zhang, W. Chu, W. Yan, Q. Xu, H. Wu, C. Wu, Y. Xie, *Adv. Mater.* **2020**, *32*, 2003251; b) Y. Wang, M. Wu, K. Wang, J. Chen, T. Yu, S. Song, *Adv. Sci.* **2020**, *7*, 2000407; c) B. Y. Guan, S. L. Zhang, X. W. Lou, *Angew. Chem., Int. Ed.* **2018**, *57*, 6176; d) S. H. Lee, J. Kim, D. Y. Chung, J. M. Yoo, H. S. Lee, M. J. Kim, B. S. Mun, S. G. Kwon, Y. E. Sung, T. Hyeon, *J. Am. Chem. Soc.* **2019**, *141*, 2035.
- [12] a) Z. Li, G. Jiang, Y. P. Deng, G. Liu, D. Ren, Z. Zhang, J. Zhu, R. Gao, Y. Jiang, D. Luo, Y. Zhu, D. H. Liu, A. M. Jauhar, H. Jin, Y. Hu, S. Wang, Z. Chen, *Science* **2020**, *23*, 101404; b) O. H. Kim, Y. H. Cho, S. H. Kang, H. Y. Park, M. Kim, J. W. Lim, D. Y. Chung, M. J. Lee, H. Choe, Y. E. Sung, *Nat. Commun.* **2013**, *4*, 2473; c) A. I. Douka, Y. Xu, H. Yang, S. Zaman, Y. Yan, H. Liu, M. A. Salam, B. Y. Xia, *Adv. Mater.* **2020**, *32*, 2002170; d) T. Sun, L. Xu, S. Li, W. Chai, Y. Huang, Y. Yan, J. Chen, *Appl. Catal., B* **2016**, *193*, 1.
- [13] a) W. Xia, M. A. Hunter, J. Wang, G. Zhu, S. J. Warren, Y. Zhao, Y. Bando, D. J. Searles, Y. Yamauchi, J. Tang, *Chem. Sci.* **2020**, *11*, 9584; b) Z. Zhu, H. Yin, Y. Wang, C. H. Chuang, L. Xing, M. Dong, Y.-R. Lu, G. Casillas-Garcia, Y. Zheng, S. Chen, Y. Dou, P. Liu, Q. Cheng, H. Zhao, *Adv. Mater.* **2020**, *32*, 2004670.
- [14] J. Wang, X. Jing, Y. Cao, G. Li, Q. Huo, Y. Liu, *CrystEngComm* **2015**, *17*, 604.
- [15] X. Jing, L. Zhang, T. Ma, G. Li, Y. Yu, Q. Huo, M. Eddaoudi, Y. Liu, *Cryst. Growth Des.* **2010**, *10*, 492.
- [16] C. Xu, Z. Lin, D. Zhao, Y. Sun, Y. Zhong, J. Ning, C. Zheng, Z. Zhang, Y. Hu, *J. Mater. Sci.* **2019**, *54*, 5412.
- [17] B. Wang, Y. Ye, L. Xu, Y. Quan, W. Wei, W. Zhu, H. Li, J. Xia, *Adv. Funct. Mater.* **2020**, *30*, 2005834.
- [18] a) X. Tang, R. Cao, L. Li, B. Huang, W. Zhai, K. Yuan, Y. Chen, *J. Mater. Chem. A* **2020**, *8*, 25919; b) S. L. Zhang, B. Y. Guan, X. W. Lou, *Small* **2019**, *15*, 1805324.
- [19] Q. Lu, J. Yu, X. Zou, K. Liao, P. Tan, W. Zhou, M. Ni, Z. Shao, *Adv. Funct. Mater.* **2019**, *29*, 1904481.
- [20] Q. Yang, Y. Jia, F. Wei, L. Zhuang, D. Yang, J. Liu, X. Wang, S. Lin, P. Yuan, X. Yao, *Angew. Chem., Int. Ed.* **2020**, *59*, 6122.
- [21] H. B. Yang, J. Miao, S. F. Hung, J. Chen, H. B. Tao, X. Wang, L. Zhang, R. Chen, J. Gao, H. M. Chen, L. Dai, B. Liu, *Sci. Adv.* **2016**, *2*, 1501122.
- [22] S. Wang, S. Zhang, *J. Inorg. Organomet. Polym. Mater.* **2017**, *27*, 1317.
- [23] a) X. Peng, L. Zhang, Z. Chen, L. Zhong, D. Zhao, X. Chi, X. Zhao, L. Li, X. Lu, K. Leng, C. Liu, W. Liu, W. Tang, K. P. Loh, *Adv. Mater.* **2019**, *31*, 1900341; b) J. Liang, X. Du, C. Gibson, X. W. Du, S. Z. Qiao, *Adv. Mater.* **2013**, *25*, 6226.
- [24] a) L. Lai, J. R. Potts, D. Zhan, L. Wang, C. K. Poh, C. Tang, H. Gong, Z. Shen, J. Lin, R. S. Ruoff, *Energy Environ. Sci.* **2012**, *5*, 7936; b) L. Liu, G. Zeng, J. Chen, L. Bi, L. Dai, Z. Wen, *Nano Energy* **2018**, *49*, 393; c) Z. Xing, R. Jin, X. Chen, B. Chen, J. Zhou, B. Tian, Y. Li, D. Fan, *Chem. Eng. J.* **2021**, *410*, 128015.
- [25] S. Xiong, M. Lin, L. Wang, S. Liu, S. Weng, S. Jiang, Y. Xu, Y. Jiao, J. Chen, *Appl. Surf. Sci.* **2021**, *546*, 149064.
- [26] a) L. Han, L. Guo, C. Dong, C. Zhang, H. Gao, J. Niu, Z. Peng, Z. Zhang, *Nano Res.* **2019**, *12*, 2281; b) J. Q. Shen, P. Q. Liao, D. D. Zhou, C. T. He, J. X. Wu, W. X. Zhang, J. P. Zhang, X. M. Chen, *J. Am. Chem. Soc.* **2017**, *139*, 1778.
- [27] X. Zhang, X. Sun, S. X. Guo, A. M. Bond, J. Zhang, *Energy Environ. Sci.* **2019**, *12*, 1334.
- [28] C. Wei, Z. J. Xu, *Small Methods* **2018**, *2*, 1800168.
- [29] a) P. Yu, L. Wang, F. Sun, Y. Xie, X. Liu, J. Ma, X. Wang, C. Tian, J. Li, H. Fu, *Adv. Mater.* **2019**, *31*, 1901666; b) Q. Lu, H. Wu, X. Zheng, Y. Chen, A. L. Rogach, X. Han, Y. Deng, W. Hu, *Adv. Sci.* **2021**, *8*, 2101438.
- [30] C. F. Li, J. W. Zhao, L. J. Xie, J. Q. Wu, G. R. Li, *Appl. Catal., B* **2021**, *282*, 119463.